arXiv:1403.2691v2 [astro-ph.GA] 12 Mar 2014

The Panchromatic Hubble Andromeda Treasury. VII. The Steep Mid-Ultraviolet to Near-Infrared Extinction Curve in the Central 200 pc of the M31 Bulge

Hui Dong[1,2], Zhiyuan Li[3,4], Q. D. Wang[2], Tod R. Lauer[1], Knut Olsen[1], Abhijit Saha[1], Julianne Dalcanton[5], Karl Gordon[6,7], Morgan Fouesneau[5], Eric Bell[8], Luciana Bianchi[9]

[1] *National Optical Astronomy Observatory, Tucson, AZ, 85719*

[2] *Department of Astronomy, University of Massachusetts, Amherst, MA, 01003*

[3] *School of Astronomy and Space Science, Nanjing University, Nanjing, 210093, China*

[4] *Department of Physics and Astronomy, University of California, Los Angeles, CA, 90095*

[5] *Astronomy Department, University of Washington, Seattle, WA, 98195*

[6] *Space Telescope Science Institute, 3700 San Martin Drive, Baltimore, MD, 21218*

[7] *Sterrenkundig Observatorium, Universiteit Gent, Gent, Belgium*

[8] *Department of Astronomy, University of Michigan, Ann Arbor, MI 48109*

[9] *Department of Physics and Astronomy, Johns Hopkins University, Baltimore, MD 21218*

E-mail: hdong@noao.edu

ABSTRACT

We measure the extinction curve in the central 200 pc of M31 at mid-ultraviolet to near-infrared wavelengths (from 1928Å to 1.5μm), using *Swift/UVOT* and *HST WFC3/ACS* observations in thirteen bands. Taking advantage of the high angular resolution of the *HST WFC3* and *ACS* detectors, we develop a method to simultaneously determine the relative extinction and the fraction of obscured starlight for five dusty complexes located in the circumnuclear region. The extinction curves of these clumps (R_V=2.4-2.5) are steeper than the average Galactic one (R_V=3.1), but are similar to optical and near-infrared curves recently measured toward the Galactic Bulge ($R_V \sim 2.5$). This similarity suggests that steep extinction curves may be common in the inner bulge of galaxies. In the ultraviolet, the extinction curves of these clumps are also unusual. We find that one dusty clump (size <2 pc) exhibits a strong UV bump (extinction at 2175Å), more than three standard deviation higher than that predicted

by common models. Although the high stellar metallicity of the M31 bulge indicates that there are sufficient carbon and silicon to produce large dust grains, the grains may have been destroyed by supernova explosions or past activity of the central super-massive black hole, resulting in the observed steepened extinction curve.

1. Introduction

Dust grains are pervasive in the Universe, absorbing, scattering and re-radiating light, affecting all wavelengths. Accounting for the effects of dust is one of the fundamental steps when inferring intrinsic properties of astrophysical objects. The degree of the effects depends not only on the total column density of dust grains, but also on their size and composition. Dust grains of various sizes affect different parts of the electromagnetic spectra. Small grains mainly absorb at shorter wavelengths, such as the ultraviolet (UV), while large grains dominate attenuation in the infrared (IR). In particular, carbonaceous grains are suggested to cause strong extinction near 2175Å (Draine 2003). The overall wavelength dependence of dust extinction is called the 'extinction law' (or extinction curve), which is conventionally expressed to be the ratio between the absolute extinction, A_λ, at some wavelength, λ and the absolute extinction in the V band, A_V, as a function of the reciprocal of the wavelength. The extinction curve is governed by the mix of dust grains, which can potentially be affected by the local environments. Strong shocks and UV photons could destroy large grains and thus change the shape of the extinction curve (Jones 2004).

Extinction curves have been extensively studied in the Milky Way (MW, Fitzpatrick 2004 and reference therein) and in the Magellanic Clouds (MCs, Large Magellanic Cloud: LMC and Small Magellanic Cloud: SMC, Gordon et al. 2003). Thanks to the International Ultraviolet Explorer (IUE), many high-quality low-resolution UV spectra of the stars in the MW and the MCs have made previous work on extinction curves possible. These studies have revealed significant environmentally-dependent effects on the extinction curves, reflected in varying UV slopes and strengths of the 2175Å bump. Cardelli et al. (1989) find that most extinction curves in the MW could be expressed with a function that depends on a single parameter, R_V=$A_V/(A_B$-$A_V)$ (A_B is the absolute extinction in the B band), which roughly traces the dust grain size. Cardelli's extinction curve steepens (i.e. the relative extinction in the short wavelength becomes large) with decreasing R_V, although deviations are found toward several directions (Mathis & Cardelli 1992). One of the most significant features of the MW extinction curve is the strong 2175Å bump, the width of which is sensitive to the local environment (from 0.63 to 1.47 μm^{-1}; Valencic et al. 2004). In contrast to the well-behaved

extinction curves in the MW, the extinction curves in the MCs, especially the SMC, are much steeper in the UV bands and exhibit a significantly weaker 2175Å bump (Gordon & Clayton 1998; Misselt et al. 1999). Gordon et al. (2003) fit the extinction curves in the MCs with the generalized model provided by Fitzpatrick & Massa (1990) (similar to that of Cardelli et al. 1989), and claim that the variation in dust properties in the MW and MCs is caused by environmental effects.

The Andromeda galaxy (M31, at a distance of ∼780 kpc; McConnachie et al. 2005) provides us with an ideal testbed to study the extinction curves in regions with different metallicity and star-forming activity. The extinction curve in the M31 disk is similar to the 'average' Galactic one (R_V=3.1), albeit with a possibly weaker 2175Å bump (Bianchi et al. 1996). Using ground-based optical images in BVRI bands, Melchior et al. (2000) find that the extinction curve of a dusty complex 1.3′ on the sky (∼300 pc in projection) northwest of the M31 nucleus is much steeper ($R_V \sim 2.1$).

In this work, we study the extinction curve in the central 200 pc of the circumnuclear region (CNR) of M31. As the second closest galactic nucleus, the CNR of M31 offers a unique laboratory (Li, Wang & Wakker 2009, and references therein) for studying the interaction and co-evolution between the super-massive black holes (SMBHs) and their host galaxies. By virtue of proximity, we can achieve an unparalleled linear resolution in M31 for a detailed study on various astrophysical activities in an extreme galactic nuclear environment. Like our Galaxy, M31 harbors a radiatively quiescent SMBH, named M31* (Dressler & Richstone 1988; Kormendy 1988; Crane et al. 1992; Garcia et al. 2010; Li et al. 2011). On the other hand, unlike the active star formation in the Galactic Center, the nuclear bulge of M31 does not host any young massive stars (less than 10 Myr old, Brown et al. 1998; Rosenfield et al. 2012) and contains only a small amount of molecular gas (Melchior et al. 2000; Melchior & Combes 2011, 2013). The stellar population in the M31 bulge is found to be highly homogeneous, dominated by old stars (∼8 Gyr, Olsen et al. 2006; Saglia et al. 2010). In the central 2′ (∼450 pc) , the two-dimensional surface brightness distribution of the bulge agrees well with a Sérsic Model (Peng 2002; Li et al. 2014). The metallicity in the M31 bulge seems to be super-solar (Saglia et al. 2010) and much higher than that of the MCs. The steep extinction curve claimed by Melchior et al. (2000) may be due to the nuclear environment of the galaxy, with its high metallicity, as well as the potential impact of the SMBH (i.e. due to ongoing mechanical feedback and/or previous outbursts) and strong interstellar shocks, all of which could affect the size and compositions of the dust grains.

Because of the relatively low line-of-sight extinction, the CNR of M31 is the nearest well-defined galaxy nucleus that can be mapped from the UV to the near-IR (NIR) bands.

To our knowledge, there has not yet been a study of the extinction curve covering the UV-optical-NIR wavelength range in the central ~ 500 pc of a normal galaxy. The understanding of the extinction curve over this entire range is essential to studies of distant galactic nuclei, especially for those with similar properties.

In this paper, we empirically derive the relative extinctions at 13 bands from the mid-UV (MUV) to NIR and then determine the extinction curves for representative regions in the CNR of M31. We utilize data from the *HST* Wide Field Camera 3 (*WFC3*) and Advanced Camera for Surveys (*ACS*) of multiple programs (Dalcanton et al. 2012; Li et al. 2014). The cores of dusty clumps can be resolved in our data, thanks to the superb angular resolution of *HST* ($<0.15''$, i.e. $\sim$0.55 pc), while the high sensitivity of the *HST WFC3* and *ACS* cameras ensures high signal-to-noise (S/N) ratios. We also utilize *Swift/UVOT* observations with three MUV filters, the middle of which covers the 2175Å bump. Therefore, the *Swift/UVOT* filters can be used not only to examine the slope of the extinction curve in the MUV, but also to probe the strength of the 2175Å bump. In a companion work, Li et al. (2014) studied the fine spatial structures of the extinction features in the CNR of M31.

We present the *Swift* and *HST* observations, and the data reduction in §2. We describe our method to derive the line-of-sight locations and the extinction curves in §3, apply it to the dusty clumps in M31's CNR in §4 and present the results in §5. We discuss the implications of our results in §6 and conclude the paper in §7.

2. Data

2.1. *HST WFC3* and *ACS* observations

We utilize images taken by *HST WFC3* and *ACS* in ten bands (see Table. 1); six bands from the Panchromatic Hubble Andromeda Treasury Survey (PHAT; Dalcanton et al. 2012, GO-12055), three bands from Program GO-12174 (Li et al. 2014), and one band from each of Programs GO-10006, GO-10760 and GO-11833 (PI: Michael Garcia). The central wavelength of the *WFC3* F547M filter (5447 Å) is close to that of the traditional Johnson V band (5400 Å). Therefore, we consider F547M as an analog of the V band in this work. The detailed description of these programs and data reduction steps are given in Dong et al. (2014) and Li et al. (2014), but we describe the key steps here. We correct for bad pixels, dark current and flat-fielding for individual dithered exposures with 'calwfc3' and 'calacs' in

'PyRAF'. We then merge exposures of each pointing position using 'Multidrizzle'[1]. We first correct for the relative astrometry among the F475W images at different pointing positions, using the χ^2 minimization, as described in Dong et al. (2011). The images of the other nine filters are aligned to the coordinate system of the F475W band. We calculate relative bias offsets of the position images in individual bands, using the same χ^2 minimization method. Because the CNR of M31 has a high surface brightness in all ten bands, we do not subtract a sky background. Using the aligned, bias corrected images, we then construct a mosaic image for each band. We match the resolution of each of the other nine filters to the poorest resolution of F160W band (FHWM, $\sim$0.15″), by utilizing point spread functions (PSFs) of the ten bands produced by 'Tinytim'[2] and 'PSFMATCH' in 'PyRAF' to produce the appropriate kernels. All the final images are rebinned to 0.13″/pixel ($\sim$ 0.5 pc /pixel), the pixel size of the WFC3/IR detector.

We use a box filter to empirically determine local background and intensity uncertainty maps, as well as to remove distinct stellar sources in our analysis (§4). The size of the box is 5×5 pixels ($\sim$0.65″×0.65″, i.e. 4.3×4.3 F160W FWHM), which is large enough to remove sources and small enough to trace local background fluctuations. The median and 68% percentage uncertainty within the box in the mosaic of each filter (n) are used to represent the local background (B_n) and its associated standard deviation (σ_n) of the central pixel of this box. The median ratios of the uncertainty to the intensity within the 0.65″×0.65″boxes are listed in Table 1 for the ten *HST* bands. The F275W, F110W and F160W bands have the lowest signal-to-noise ratio (SNR), because of either the short exposure time (F275W) or the stochastic uncertainty due to the presence of unresolved red giant branch (RGB) and asymptotic giant branch (AGB) stars, which are bright in the near-IR bands (F110W and F160W). We identify the pixels with intensity larger than B_n+3σ_n in at least one of the ten *HST* bands, as 'source' pixels. We remove each of these pixels as well as their immediate neighbors (i.e., a 3x3 box, $\sim$ 2.5×2.5 F160W FWHM) to avoid the contamination from the wing of bright sources.

2.2. *Swift/UVOT* Observations

Swift/UVOT is a 30 cm UV and Optical telescope on board the *Swift* spacecraft (Roming et al. 2005). In this work, we use the three MUV filters of *Swift/UVOT*: UVW2, UVM2, UVW1

[1]'PyRAF' and 'Multidrizzle' are the product of the Space Telescope Science Institute, which is operated by AURA for NASA.

[2]http://www.stsci.edu/hst/observatory/focus/TinyTim

(see Table 1). The UVM2 filter encompasses the 2175Å bump, while the other two filters (UVW2 and UVW1) cover the blue and red sides of the bump, respectively. These three filters have a strong effect on constraining extinction curves, because various extinction curves have the largest differences in the slopes of the extinction curves in the UV band and in the strength of the 2175Å bump. UVW1 is close to *WFC3* F275W. Because UVW2 and UVW1 have extended red tails (the 'Red Leak' problem) and the M31 bulge is bright in the optical and the NIR, the effective wavelengths and thus the relative extinction (A_λ/A_V) of the two bands are sensitive to the age and metallicity of the background stellar populations (see Appendix A). In §5, we describe a method to compare the relative extinction derived from our observation with the ones predicted by different extinction curves. The angular resolution of *Swift/UVOT* in the MUV ($\sim$2.5″) is poorer than that of *HST* observations (<0.15″), but is still better than *GALEX* (4″- 5″) (Morrissey et al. 2007). To reduce the amount of telemetry from the spacecraft, all of the observations in image mode have already been binned by a factor of 2, with a pixel scale of 1″ pixel^{-1} ($\sim$3.8 pc pixel^{-1}). After excluding several observations with exposure time shorter than 20 seconds, the total exposures times are 106, 46 and 153 kilo-seconds for the UVW2, UVM2 and UVW1 filters, respectively.

We process the data using the steps described in the UVOT Software Guide. First, we reproduce the level I products with the UVOT FTOOLS (HEAsoft 6.12). Second, we rectify the 'coincidence loss' problem (a problem in which the UVOT camera counts only one photon, even if there are more than one photon arriving at the same CCD pixel in one readout frame) by using Fig. 6 of Breeveld et al. (2010). We remove pixels with intensity >0.4 counts s^{-1} pixel^{-1}, for which the correction for coincidence loss is large and uncertain. Fortunately, we find that only the central $< 5''$ (19 pc) of M31 and the cores of several bright foreground stars are removed, even in the UVW1 band, which has the biggest chance of suffering from the coincidence loss problem. Third, we manually remove the 'smoke rings' found in the UVW2 and UVW1 observations, using an annulus with 30″ and 140″ for the inner and outer radii (see also Fig. 20 of Breeveld et al. 2010). Fourth, we derive the relative astrometry between individual exposures of each filter, using χ^2 minimization as in Dong et al. (2011) to correct for the relative astrometry between individual exposures of each filter before producing final mosaics. The bright UV stars in the *Swift* observations are used to align the final mosaics to the coordinate system of the *HST* observations. Fifth, we construct the PSF for the three filters, using relatively bright UV stars (but without the 'coincidence loss' problem).

3. Method

In this section, we describe our method to constrain the extinction curves of individual dusty clumps identified in the CNR of M31. We first review two conventional methods and their limitations if they were applied to the M31 bulge, and a third method adopted in our companion work (Li et al. 2014). The widely used 'standard pair' method (Massa et al. 1983) compares the spectra of pairs of stars of a similar spectral type, but one with high absolute extinction and the other not. Early-type stars (usually O or B) are generally used, because they are bright in the UV. Bianchi et al. (1996), for example, apply this method to young massive stars in some OB associations of the M31 disk. The method cannot be used here, because such stars are absent in the CNR of M31 (e.g., Brown et al. 1998; Rosenfield et al. 2012).

An alternative method is to use integrated light to derive the extinction curve. Elmegreen (1980) is among the first to employ such a method in several spiral galaxies. Walterbos & Kennicutt (1988) and Melchior et al. (2000) apply a similar method to study dust extinction in the disk and the bulge of M31, respectively. In particular, Melchior et al. (2000) focus on the dust complex D395A/393/384, located at $\sim$1.3$'$ northwest of the M31* and derive the optical extinction curve, $\langle A\rangle/(\langle A_B\rangle\text{-}\langle A_V\rangle)$, from the mean extinctions ($\langle A\rangle$) in four bands (BVRI). However, this work is forced to assume the fraction, f, of obscured starlight, due to the lack of the information about the line-of-sight locations of this dusty clump. Recently, Li et al. (2014) use the same *HST* dataset here to directly constrain the pixel-by-pixel values of f for various dusty clumps in the M31's CNR, assuming that they are all located in a thin plane embedded in a triaxial ellipsoid bulge (Stark 1977).

Here, we employ an alternative approach, relaxing the geometric assumptions made by Li et al. (2014). Because the filling factor of dusty clumps is low (see Dong et al. 2014; Li et al. 2014), it is reasonable to assume that they are relatively isolated individual features, with each cloud occupying a single depth inside the bulge and that their sizes (and hence thicknesses) are small compared to the bulge depth. Therefore, for a single dusty clump, the fraction of starlight behind the dusty clump can be treated as a constant and in our approach, we consider a single f value per each dusty clump.

For one pixel in the mosaic of the n^{th} filter, we calculate the ratio $\Re_n$ between the observed intensity I_n, the intrinsic intensity S_n, given by the fraction of obscured starlight

f_n and the absolute extinction[3] A_n in Eqn. 1.

$$\Re_n = \frac{I_n}{S_n} = (1 - f_n) + f_n \times 10^{-0.4 \times A_n} \quad (1)$$

The terms $(1-f_n)$ and $f_n \times 10^{-0.4 \times A_n}$ are the fractions of unobscured and obscured starlight, respectively. I_n is from the observations in §2 and we derive S_n, using the method detailed in §4.1. This equation neglects the starlight scattered into the line of sight, which we show is a safe assumption in Appendix C. In Fig. 1, we depict the non-linear relationship between f_n and A_n for different $\Re_n$. We see that f_n is anti-correlated with A_n. At small f_n, A_n is sensitive to f_n, but changes slowly when $f_n > 0.8$. For a fixed $\Re_n$ value, simply assuming f_n=1 for a dust clump in very extinguished regions, we could potentially bias ourselves towards underestimating the actual extinction, A_n.

We can convert Eqn. 1 into a canonical extinction curve by normalizing the extinction in band n to the extinction in our nominal V-band proxy, F547M, assuming that the extinction curve is constant within each dusty clump. If we define the ratio of extinctions as $\frac{A_n}{A_{F547M}} \equiv \Gamma(n, F547M)$ [or Γ(n) for simplicity, unless otherwise noted] and assume that f is the same for all filters ($f_n = f_{F547M} = f$), we can eliminate the absolute extinction A_{F547M} to obtain the following equation for each individual pixel (k):

$$\Re_n - 1 + f = f^{1-\Gamma(n)} \times (\Re_{F547M} - 1 + f)^{\Gamma(n)} \quad (2)$$

We can then estimate, the fraction of obscured starlight, f, and the relative extinction, $\Gamma(n)$, for each dusty clump, by minimizing the following:

$$\chi^2 = \sum_k \sum_n \frac{[\Re_n - 1 + f - f^{1-\Gamma(n)} \times (\Re_{F547M} - 1 + f)^{\Gamma(n)}]^2}{(\frac{\sigma_n}{I_n})^2 + (\frac{\sigma_{F547M}}{I_{F547M}})^2 + (\frac{\delta S_n}{S_n})^2 + (\frac{\delta S_{F547M}}{S_{F547M}})^2} \quad (3)$$

where $\sum_k$ and $\sum_n$ are the sum over all the pixels and over the included bands (see §4) for a given dusty clump. The variables σ_n and σ_{F547M} are the photometric uncertainties of I_n and I_{F547M}, respectively, as determined in §2.1. The variables δS_n and δS_{F547M} are the uncertainties of S_n and S_{F547M}, determined in §4.1.

4. Analysis

We apply the above method to the *Swift*/*UVOT* and *HST* data. We are primarily interested in the dusty clumps within the central 10″ (38 pc) to 60″ (227 pc), a region that

[3]Due to the broadness of the filters, their effective wavelengths are sensitive to the background stellar light (see Appendix A). We use A_n, instead of A_λ to represent the absolute extinction within the n^{th} filter.

has drawn relatively little attention in previous studies. For each clump, we assume that the obscured fraction f is a constant among the different bands (Li et al. 2014), the included satisfying the requirement of Eqn. 2.

In Fig. 2, we show the *HST*/*WFC3* F336W intensity map (Fig. 2a) and the intensity ratio map between F160W and F336W (Fig. 2c) in the central $2' \times 2'$ of the M31 bulge. This ratio is sensitive to extinction, as well as age and metallicity of local stellar populations, in the sense that large extinction, old age, or high metallicity could enhance this ratio. The majority of the field of view seems to be free of patchy extinction. We use cyan boxes to mark five dark and fuzzy structures in the intensity ratio map; these structures have low F336W intensity and should indicate sites of genuine high extinction. The locations and sizes of these five cyan boxes are given in Table. 2. Due to their low surface density ($< 10^{21}$ H cm^{-2}, Li et al. 2014), these five regions do not have available CO detections yet. In the extinction map presented by Li et al. (2014), these five regions include many high extinction regions that appear isolated from each other. The high intensity ratio in the central $10''$ is more likely caused by the nucleus having a stellar population different from that of the rest of the M31 bulge (see Dong et al. 2014), rather than significant extinction variations given that previous studies do not find molecular clouds in the same central $5''$ (19 pc) region of M31.

We first describe how to construct the intrinsic surface brightness distribution of the M31 bulge in §4.1 and in §4.2, we define our selection criteria on individual pixels to define dusty clumps. We then minimize the χ^2 (Eqn. 3) in two steps, first using only *HST* images (§4.3). We then extend in §4.4 the minimization to including *Swift* images after correcting for the unresolved sources and differential extinction within the larger pixels of *Swift* based on *HST*-only derived values. Finally, we address several caveats of our analysis in §4.5.

4.1. Intrinsic Light Distribution in the M31 Bulge

We fit the surface brightness distribution, using the surface photometry algorithm described in Lauer (1986) to determine S_n for each filter. This algorithm is similar to the '`ellipse`' task in 'IRAF' (Jedrzejewski 1987). It first divides an image into a set of concentric annuli centered on M31*. The width of these annuli increases by 0.1 in a log scale. The surface brightness distribution of each annulus is fit with an ellipse. The normalization, ellipticity, and position angle of each annulus is solved simultaneously, using a non-linear χ^2 minimization method. Similarily to sigma-clipping, we iteratively flag and then mask pixels of dusty clumps, detector artifacts and discrete sources to refine our fit of the intrisic light profile. After the parameters of ellipses for individual annuli are derived, we recover the in-

trinsic surface brightness distribution, S_n, in each filter image. Because of the large number of pixels and high SNR data, the statistical uncertainty of S_n, within a given annulus, δS_n, is typically of 0.2%, much smaller than the photometric uncertainty of a single pixel (i.e. σ_n). In Fig. 3, we depict the distribution of I_n/S_n in the central $2'\times2'$ ($\sim$450 pc$\times$450 pc) of the M31 bulge in the F275W, F547M and F814W bands. The respective dispersions of the distributions of I_n/S_n (0.086, 0.035 and 0.058) are similar to the photometric uncertainties in the three bands (σ_n, see Table. 1).

4.2. Identifying Pixels Associated with Dusty Clumps

When fitting the extinction curve, we select only those pixels with strong extinction, which we refer to as 'dusty' pixels. For each band, the histogram of the pixel values in the $\Re_n$ map within the central $2'\times2'$ ($\sim$450 pc$\times$450 pc) is well fit with a Gaussian distribution. Because the filling factor of the dusty clumps is small in the M31 bulge, the centroid of the Gaussian distribution is around one and the standard deviation is dominated by the photometric uncertainty. The extra pixels at the wings of the Gaussian curve are due to bright sources (large $\Re_n$) or high extinction (small $\Re_n$), which cannot be reproduced by the method in §4.1. The 'dusty' pixels are chosen to have I_n/S_n two standard deviations below one in all the UV and optical bands (i.e., F275W, F336W, F390M, F435W, F475W, F547M). If f=1, using Eqn. 1, this threshold then corresponds to $A_{F275W} > 0.2$ or $A_{F547M} > 0.04$. With the threshold, fewer than 1.5% of the pixels are expected to be randomly below this limit and thus the pixels passing this cut almost certainly suffer strong extinction. In contrast, in the images at longer wavelength, the ratio is mostly determined by the photometric uncertainty and only a few pixels with very high extinction could have ratios significantly below one. The same 'dusty' pixels are used for all the filters in the following analysis.

4.3. Constraining f with the *HST* Observations

We use Eqn. 3 to derive the fraction of obscured starlight, f, and the extinction relative to the V band, $\Gamma(n)$, for the five dusty clumps as defined in Fig. 2c. Using the 'MPFIT' package (Gradient descent, Markwardt 2009), we simultaneously fit the F336W, F390M, F435W, F475W bands, since the intensities in these bands are most sensitive to the extinction. The F275W band is excluded because of the large statistic photometric uncertainty (see Table 1). Because $\Re_n$ is typically close to 1 at near-IR wavelengths, the fraction of obscured starlight, f, is very insensitive to the absolute extinction. Including the longest wavelength bands in

the fitting will introduce large uncertainty into f and thus into the relative extinction. A Monte Carlo method is then used to evaluate the uncertainties in f and $\Gamma(n)$. For each pixel, we randomly add a value which follows a normal distribution with a mean of zero and a standard deviation equal to $\frac{\sigma_n}{S_n}$ and $\frac{\sigma_{F547M}}{S_{F547M}}$ into $\Re_n$ and $\Re_{F547M}$, respectively. We rerun 'MPFIT' 1000 times to obtain the 68% percentage uncertainty of the f and $\Gamma(n)$, as listed in Table 3.

Fig. 4 illustrates two examples of our fitting results for Clump A and Clump D. The top panels show $\Re_{F336W}$ versus $\Re_{F547M}$ for all the 'dusty' pixels in each cloud. The bottom panels show the χ^2 distribution as the function of f and $\Gamma(F336W)$. The best-fit parameters show that the two clouds have similar $\Gamma(F336W)$, but different f. To show the sensitivity of the data to different values of f and $\Gamma(F336W)$, in the top panels of Fig 4, we also compare the observed data points with the curves predicted by various f and $\Gamma(F336W)$. For those 'dusty' pixels with relatively low absolute extinction (such as $\Re_{F547M} > 0.85$), the relationship between $\Re_{F336W}$ and $\Re_{F547M}$ is not sensitive to f, but constrains the $\Gamma(F336W)$ well; Instead, the constraints on f come purely from the most attenuated pixels.

The derived f could be used as an indicator of the line-of-sight locations of the dusty clumps in the M31 bulge. Our results show that the two dusty clumps (Clump A and D, $f > 0.5$) are in front of the M31*, whereas the other two (Clumps B and E, $f < 0.5$) are behind, as summarized in Table 3. Clump C ($f \sim 0.5$) is at the middle. The uncertainties of f for Clump C and Clump D are relatively large, because the former has the smallest number of 'dusty' pixels, whereas the latter does not have high enough extinction (see Fig. 1).

Using the 'best-fit' values of f, we derive A_{F547M} from Eqn. 1. The median A_{F547M} values and their 68% quantile for the five dusty clumps are 0.25±0.10, 0.50±0.18, 0.31±0.08, 0.18±0.08 and 0.56±0.20, respectively. The histograms of A_{F547M} for these five dusty clumps are presented in Fig. 5. The A_{F547M} distributions of Clumps B and E, having more high extinction pixels, appear flatter than those of Clumps A, D and E.

We fix the value of f in Eqn. 3 and use 'MPFIT' to derive the relative extinction $\Gamma(n)$ for the other *HST* filters (F275W, F665N, F814W, F110W, F160W), using the same Monte Carlo method to derive the uncertainty of $\Gamma(n)$. We computed the effect of uncertainty in f on $\Gamma(n)$ by deriving the values of $\Gamma(n)$ corresponding to the best-fit $f \pm \delta f$ (δf is the uncertainty in f). We then add half of the difference between the derived values of $\Gamma(n)$ in quadrature to the uncertainty derived from the Month Carlo method with f fixed at its best-fit value to give the total variance in $\Gamma(n)$. The results are listed in Table. 3.

4.4. The Correction for *Swift/UVOT* Data

We next use the *Swift/UVOT* images at the three MUV bands to constrain the extinction curve at shorter wavelengths. We first match the *HST/ACS* PSF to that of *Swift/UVOT*. Since the PSF of the *Swift/UVOT* is much larger than that of the *HST* (see §2), we simply convolve the *HST* mosaics with the PSF of *Swift/UVOT* derived in §2.2. We still use the same bands in §4.2 to select out the 'dusty' pixels. The intrinsic intensity distributions at these three UV filters are also derived using the method of Lauer (1986).

The contribution from unresolved sources in the three *Swift/UVOT* filters could potentially bias the extinction curve in the MUV bands. Due to the relatively poor angular resolution and low signal-to-noise ratio, no 'source' pixel is found in *Swift/UVOT* images of the five dusty clumps. Moreover, because the M31 bulge is relatively dim in the MUV bands, single UV bright stars can dominate the integrated intensities of individual pixels. As a result, we would overestimate $\Re_n$ in the MUV bands and underestimate the extinction, leading to flattened extinction curves. To minimize this effect, we first use the *HST* F275W band, which covers a comparable wavelength, to estimate the source contribution in each pixel of the *Swift/UVOT* images. We downgrade the resolution of the *observed* F275W band images with and without the 'source' pixels defined in §2.1 by convolving them with the *Swift/UVOT* PSF and rebinning into the pixel size of the *Swift/UVOT* observations ($1''$ pixel^{-1}). The ratio map between these two images represents the fraction of 'bright source-free' emission in individual *Swift/UVOT* pixels. The mean contribution of the point sources in the fields of the five dusty clumps is between 27% to 42%. We then multiply the corresponding ratio map to the observed *Swift/UVOT* UV images to remove the 'source' contamination. To make sure that we compare the observed and intrinsic intensities at the same sky area, we also need to remove the intensity contribution of the 'source' pixels from individual pixels in the intrinsic *Swift/UVOT* UV images. We produce a similar ratio map for the intrinsic F275W image, S_n, (see §4.1), which is then multiplied to the intrinsic intensity distributions of the *Swift/UVOT* UV images. The resultant observed and intrinsic 'bright source-free' intensity images are used to derive the $\Re_n$. After these corrections for point source contamination, the $\Re_n$ of the *UVOT* bands decreases, the relative extinction compared to the V-band increases by a factor of 1.2-1.8 and the extinction curve becomes steeper.

Differential extinction within one *Swift/UVOT* pixel could also flatten the extinction curve at the short wavelengths ('flattening bias'; see also Calzetti et al. 2000), due to unresolved structures in the dust below the angular scale of the pixel. From the *HST* images, we know that the extinction can change sharply on arcsecond scales (see Fig. 2 and Dong et al. 2014; Li et al. 2014). The low resolution of *Swift/UVOT* tends to lose this spatial informa-

tion. As a result, the intensity in a *Swift/UVOT* pixel may be dominated by regions with the least extinction. If we just simply derived the extinction from the $\Re_n$ (i.e. Eqn. 1), we would average the extinction within one *Swift/UVOT* pixel weighted by their observed intensity, and thus we would underestimate the local extinction. This effect would lead to the flattening of the inferred extinction curve, especially at short wavelengths. We correct for this bias in the three UV bands, using the method of Fritz et al. (2011). The basic idea is that we can use the high resolution extinction map of the adjacent *HST* filters, such as F336W, to mimic those of the three MUV filters. The method is detailed in Appendix B. The results, i.e. $\Gamma(n, F336W)$ for UVW2, UVM2 and UVW1 are listed in Table 4. After this correction, $\Gamma(n, F336W)$ increases from $\sim$1.02 (Clump D) to $\sim$1.3 (Clump B). $\Gamma(n)$ is derived by multiplying $\Gamma(n, F336W)$ to $\Gamma(F336W, V)$ and is listed in Table 3. The errors of $\Gamma(n, F336W)$ and $\Gamma(F336W, V)$ are propagated into the uncertainty of $\Gamma(n)$.

4.5. Caveats

We describe four caveats of the analysis procedure described above: the foreground Galactic extinction, the filter dependence of f, the scattered light and reddening substructures on scales below the *HST* resolution. All the errors introduced by these caveats are summarized in Table. 5.

4.5.1. Foreground Galactic Extinction

What effect may the foreground Galactic extinction have on our measurements? In §4.1, we estimated the intrinsic intensity, S_n, in the field of the dusty clumps from the apparently extinction-free regions in the CNR of M31, which are, however, subject to Galactic extinction. Provided that the Galactic extinction does not vary significantly within the field-of-view, this effect cancels in $\Re_n = \frac{I_n}{S_n}$. The choice of high extinction pixels in §4.2 also reduces the effect introduced by potential variation in the Galactic extinction between I_n and S_n regions. The median A_{F547M} of the 'dusty' pixels in the clumps are larger than 0.18 mag. By constrast, the Galactic absorption toward the M31 nucleus is 0.17 (Schlafly & Finkbeiner 2011). Therefore, even a 10% fluctuation of the foreground Galactic extinction within the central region of the M31 bulge would cause only <10% error in A_{F547M}.

4.5.2. Dependence of the Fraction of Obscured Starlight on Wavelength

The fraction of obscured starlight f could vary among the filters, because of potential stellar color variation across the M31 bulge. Such variation among different filters ($|\frac{f_n - \langle f_n \rangle}{\langle f_n \rangle}|$, where $\langle f_n \rangle$ is the mean of f_n for each of the dusty clumps) appears to be small. The maximum difference among the ten *HST* filters is 2.7%, 7.1%, 1.8%, 4.7% and 5.7% for Clump A, B, C, D and E, respectively. The relatively large variation seen in Clump B is due largely to the F275W band. Excluding it, the variation of f_n decreases to 4.9%. Therefore, the F275W band provides a good test of the effect of f on the relative extinction $\Gamma(F275W)$. We find that if we were to increase f(F275W) by 7%, $\Gamma(F275W)$ would decrease to 2.79 from 2.99, or a change of only 6.7%, which is well within the uncertainty range of f of the clump.

4.5.3. Scattered Light

The observed intensity is the sum of the absorbed (background), unabsorbed (foreground) and scattered stellar light. The scattered intensity depends on dust optical depth and scattering properties (albedo and scattering phase function). In Appendix C, we run a simulation. We put a dusty clump with different column densities and locations into the M31 bulge to derive the fraction of the scattered light in the total intensity. Our results show that for our five dusty clumps, the contribution of the scattered light is less than 5%, even in the MUV bands and that the f and $\Gamma(n)$ values changed by less than 5%, if the contribution is accounted for.

4.5.4. Unresolved Reddening Structure in One HST Resolution Element

A dusty cloud likely has a fractal structure on all scales and extinction variations should exist on scales smaller than one our *HST* resolution element, i.e. $0.13''$ $\sim$0.5 pc. This could bias our extinction curve (see also, §4.4). To examine this effect, we use the extinction map of the nearby Orion A and B molecular clouds, kindly provided by Jouni Kainulainen. Kainulainen et al. (2009) have used the NIR color excess of background stars to map out the extinction distribution in the clouds. Because of their proximity (414$\pm$7 pc, Menten et al. 2007), the physical size of one pixel in these extinction map is 0.18 pc ($1.5'$) and is roughly three times better than that of our *HST* mosaics in the M31 bulge. By using the steps listed in Appendix D, we find that the structure of the extinction variation in one *HST* resolution element just introduces less than 3% and 2% uncertainties into the f and $\Gamma(n)$ values.

5. Results

The extinction curves, expressed in terms of A_n/A_{F547M}, for the five dusty clumps are shown in Fig. 6. We also provide the extinction curve averaged over the five dusty clumps. Although F275W and UVW1 are from different detectors, the similarity of the relative extinctions in these two bands is apparent and demonstrates the reliability of our correction in §4.4. Because of the 'Red Leak' problem, the effective wavelength of the UVW1 is shifted to longer wavelengths, which explains why the relative extinction in the UVW1 band is slightly smaller than that in the F275W band.

In Fig. 6, we compare the extinction curves in the five dusty clumps with those of the MW and the MCs, as well as with the results of Melchior et al. (2000). In the optical bands, our extinction curves match the three empirical extinction curves well, while the relative extinction curve (A_n/A_V) of Melchior et al. (2000) is steeper than ours (see the middle right panel of Fig. 6). Our relative extinctions in the two NIR bands (F110W and F160W) are larger than those of the MW and the MCs. But, because the absolute extinction in the clumps is not large, giving little constraints on the extinction curve in the NIR, we do not include these two bands in the subsequent quantitative analysis. Our extinction curve increases steeply in the UV bands (F275W to UVW2), compared to that of the MW. The variations of A_n/A_{F547M} among the five dusty clumps in the *Swift/UVOT* UV bands are substantial. However, the accuracy of A_n/A_{F547M} in these three bands is limited by the poor angular resolution and sensitivity of the *Swift/UVOT*.

We fit the extinction curves $\Gamma(n)$ in Fig. 6 with Fitzpatrick (1999) models, which parameterize the shape of the extinction curve, including the possible 2175Å bump. Because some of the filters have the 'Red Leak' problem, their effective wavelengths are uncertain. We thus instead calculate the inferred extinction curves (i.e. $\Gamma(n)_m$) that would be measured in the filters. We first use the best-fit stellar population model in the unobscured regions (Dong et al. 2014), to calculate the spectral energy distribution (SED) within each filter band pass. We then use the same model to obtain the SED attenuated with the Fitzpatrick (1999) models to calculate $\Gamma(n)_m$. We consider values of $1.5< R_V <4.5$ (with a step size of 0.1, while the other parameters are fixed) to minimize $\chi^2 = \sum_n \frac{(\Gamma(n)-\Gamma(n)_m)^2}{(\delta\Gamma(n))^2}$, where the sum is over the filters from UVW2 to F814W and the variable $\delta\Gamma(n)$ is the uncertainty of $\Gamma(n)$. The final R_V in the extinction model of Fitzpatrick (1999), ranging from 2.4-2.5 for the five dusty clumps, are listed in Table. 3. We use our Monte Carlo method to derive the uncertainty of R_V (δR_V). In Table. 3, we also give the R_Vs for the extinction model of Cardelli et al. (1989), for comparison with the result of the inner Galactic Bulge of Nataf et al. (2013) in §6.

The average R_V values of the five dusty clumps with the extinction model of Fitzpatrick

(1999) is 2.4±0.05, which are significantly smaller than the average Galactic R_V (3.1; Fitzpatrick 2004), and is even slightly steeper than the SMC extinction curve (R_V=2.74±0.13; Gordon et al. 2003). The comparison between our observed Γ(n) and those predicted by Fitzpatrick (1999) with the corresponding R_V is presented in Fig. 7. The model fits the observed extinction curves well in the optical, with large deviations in the UV bands (from U to UVW2). The clumps also show different degrees of agreement with the Fitzpatrick (1999) extinction curves. Clump A matches the model well, whereas Clumps B and E agree only within their respective $\delta\Gamma(n)$ for the three *Swift/UVOT* UV filters, but show less overall agreement than Clump A. For Clumps C and D, however, the observed Γ(n) of the three *Swift/UVOT* filters are systematically larger than those predicted by the model and especially, for Γ(UVM2), by more than $2\delta\Gamma(n)$ (Clump C, $2.4\delta\Gamma(n)$ and Clump D, $3.0\delta\Gamma(n)$). In spite of these variations, the average extinction curve is well fit by the Fitzpatrick (1999) model in most of the bands, although a significant enhancement in the UVM2 is apparent.

6. Discussion

The extinction curve is determined by the size and compositions of dust, which could be related to many factors, such as the metallicity of a molecular cloud and its environment. The metallicity alone is unlikely to be able to explain the variations among the extinction curves in the MW and the MCs. Different sightlines that have similar metallicity gas can show very different extinction curves. Indeed, the extinction curves toward a few lines of sight in the MCs are found to be similar to the Galactic extinction curve (Gordon et al. 2003), whereas sightlines toward four stars in the Milky Way have steep extinction curves that lack the 2175Å bump (Valencic et al. 2004). Therefore, factors other than metallicity must play important roles in determining the shape of an extinction curves. Gordon et al. (2003) point out that the differences between the MW and the MCs extinction curves may be due to their sampling different environments. In particularly, most of the studied extinction curves in the MCs are from active star-formation regions, where strong shocks and UV photons may conspire to destroy large dust grains, whereas, those in the MW are typically toward runaway main-sequence OB stars. Within M31, the metallicity in the bulge is comparable to regions of the disk (Rosolowsky 2007), for which Bianchi et al. (1996) have derived shallower extinction curves. Therefore, unless the clouds are due to accreted low metallicity gas, it seems unlikely that metallicity is responsible for those steep curves.

We have found that the extinction curves in the CNR of M31 are steep. We naively expected that the extinction curve there should be similar to or even flatter than the MW one, because of their comparable metallicity and low star formation rate, but found just the

opposite. In fact, the CNR of M31 is not the only galactic bulge with steep extinction curves in the Local Group. The Galactic inner bulge has recently been suggested to have a similar non-standard optical extinction curve (Udalski 2003; Sumi 2004; Revnivtsev et al. 2010; Nataf et al. 2013). These authors use red clump stars as standard candles, due to their nearly constant magnitude and color at high metallicities. They derive the foreground extinction in the optical and NIR bands (V, I, J and K) from the differences of the observed and intrinsic magnitudes/colors of the red clump stars toward different sightlines in the Galactic Bulge. They find that the relative exinction could not be explained by the standard Galactic extinction curve (R_V=3.1), and must instead be steeper. Nataf et al. (2013) report a value of R_V=2.5 toward the Galactic Bulge, with the extinction curve model of Cardelli et al. (1989), which is similar to the R_V value we have obtained in the CNR of M31. This consistency suggests that a steep extinction curve could be common in galactic bulges.

The extinction curves could be steepened by eliminating large grains. It is possible that they have been destroyed by interstellar shocks. Recombination lines (Hα, [N II], [S II], [O III]) have been found in the CNR of M31 by Jacoby et al. (1985) and arise from regions that are morphologically similar to that of the dust emission (Li, Wang & Wakker 2009). Therefore, the recombination lines are from the surfaces of the dusty molecular clouds. Because the [N II] line is stronger than the Hα line, these recombination lines are suggested to be excited by shocks (Rubin & Ford 1971). We speculate that the shocks from supernova explosions or past activity of M31* have evaporated large dust grains and steeped the extinction curve. For example, recently, Phillips et al. (2013) find that the interstellar medium of host galaxies surrounding 32 Type Ia supernovae has $R_V < 2.7$ with a mean value of 2.06.

We also find the 2175Å bump in our extinction curves, which is generally thought to be due to small graphite grains. The 2175Å bump is especially strong in the extinction curve of Clump D, or probably Clump C. The former is located 30″ (113 pc in projection) southeast of the D395A/393/384 clump studied by Melchior et al. (2000). This small and compact clump core has a size < 2 pc (Li et al. 2014) and appears dark in the *HST* F275W, F336W and F390M images, consistent with its high f value. The high metallicity of the clump may provide the necessary carbon and silicon to construct small graphite grains. Among the five dusty clumps, Clump D seems to have the smallest median A_{F547M}, but the largest 2175Å bump. The 2175Å bump is weaker in the extinction curve of Clump B or E, which both have high A_{F547M}. This situation is probably reminiscent of the four lines of sight in the MW (Valencic et al. 2004) through dense molecular clouds, which have weak 2175Å bumps, for example, HD62542 (A_V=0.99±0.14) and HD210121 (A_V=0.75±0.15).

Future *HST*/STIS spectra in the mid-ultraviolet range are needed to confirm the po-

tential 2175Å bump in Clumps C and D. Because of the 'Red Leak' problem and old stellar population in the M31 bulge, we need to assume the SED to compare the observed relative extinction in thirteen bands with the model. With the UV spectra, we can directly derive the extinction curve, as well as the parameters of the 2175Å bump, such as, its centroid and width.

7. Summary

In this paper, we have presented the first study of the extinction curve within the central $1'$ region of M31 from the MUV to the NIR. We have used *Swift/UVOT* and *HST WFC3/ACS* observations in thirteen bands to simultaneously constrain the line-of-sight locations and the relative extinction A_n/A_{F547M} of five dusty clumps in this region. Instead of fixed certain line-of-sight locations for these clumps, we have developed a method to determine their background stellar light fraction (f) directly from the observations.

We have shown that the extinction curve is generally steep in the circumnuclear region of M31, where the metallicity is super-solar. The derived R_V=2.4-2.5 is similar to that found toward the Galactic Bulge. We discuss this consistency which leads us to conclude that large dust grains are destroyed in the harsh environments of the bulges, e.g., via potential shocks from supernova explosions and/or past activities of M31*, as indicated by the strong [NII] recombination lines from the dusty clumps.

The extinction curves of the five dusty clumps show significant variations in the mid-ultraviolet. Some of the extinction curves can be explained by the extinction curve model of Fitzpatrick (1999). Others, most notably Clump D (probably also Clump C), shows an unusually strong 2175Å bump, which is weak elsewhere in the M31 disk (Bianchi et al. 1996).

Acknowledgments

We thank the anonymous referee for a thorough, detailed, and constructurive commentary on our manuscript. We are grateful to Bruce Draine for many valuable comments on the dust scattering. H. D. acknowledges the NASA support via the grant GO-12055 provided by the Space Telescope Science Institute, which is operated by the Association of Universities for Research in Astronomy, Inc., under NASA contract NAS 5-26555. Z. L. acknowledges support from NASA grant GO-12174 and NSFC grant 11133001.

REFERENCES

Beaton, R. L., Majewski, S. R., Guhathakurta, P., et al. 2007, ApJ, 658, L91

Baes, M., & Gentile, G. 2011, A&A, 525, A136

Bender, R., Kormendy, J., Bower, G., et al. 2005, ApJ, 631, 280

Bianchi, L., Clayton, G. C., Bohlin, R. C., Hutchings, J. B., & Massey, P. 1996, ApJ, 471, 203

Breeveld, A. A., Curran, P. A., Hoversten, E. A., Koch, S., Landsman, W., Marshall, F. E., Page, M. J., Poole, T. S., et al. 2010, MNRAS, 406, 1687

Brown, T. M., Ferguson, H. C., Stanford, S. A., & Deharveng, J.-M. 1998, ApJ, 504, 113

Calzetti, D., Armus, L., Bohlin, R. C., et al. 2000, ApJ, 533, 682

Calzetti, D. 2001, PASP, 113, 1449

Cardelli, J. A., Clayton, G. C., & Mathis, J. S. 1989, ApJ, 345, 245

Cartledge, S. I. B., Clayton, G. C., Gordon, K. D., et al. 2005, ApJ, 630, 355

Crane, P. C., Dickel, J. R., & Cowan, J. J. 1992, ApJ, 390, L9

Dalcanton, J. J., Williams, B. F., Lang, D., et al. 2012, ApJS, 200, 18

Dong, H., Wang, Q. D., Cotera, A., et al. 2011, MNRAS, 417, 114

Dong, H. et al. (2014) in preparation

Draine, B. T. 2003, ApJ, 598, 1017

Dressler, A., & Richstone, D. O. 1988, ApJ, 324, 701

Elmegreen, D. M. 1980, ApJS, 43, 37

Fitzpatrick, E. L., & Massa, D. 1990, ApJS, 72, 163

Fitzpatrick, E. L. 1999, PASP, 111, 63

Fitzpatrick, E. L. 2004, Astrophysics of Dust, 309, 33

Fritz, T. K., Gillessen, S., Dodds-Eden, K., et al. 2011, ApJ, 737, 73

Garcia, M. R., Hextall, R., Baganoff, F. K., et al. 2010, ApJ, 710, 755

Groves, B., Krause, O., Sandstrom, K., et al. 2012, MNRAS, 426, 892

Gordon, K. D., & Clayton, G. C. 1998, ApJ, 500, 816

Gordon, K. D., Clayton, G. C., Misselt, K. A., Landolt, A. U., & Wolff, M. J. 2003, ApJ, 594, 279

Gordon, K. D., Cartledge, S., & Clayton, G. C. 2009, ApJ, 705, 1320

Jacoby, G. H., Ford, H., & Ciardullo, R. 1985, ApJ, 290, 136

Jedrzejewski, R. I. 1987, MNRAS, 226, 747

Jiang, P., Zhou, H., Ji, T., et al. 2013, AJ, 145, 157

Jones, A. P. 2004, Astrophysics of Dust, 309, 347

Kainulainen, J. T., Alves, J. F., Beletsky, Y., et al. 2009, A&A, 502, L5

Kormendy, J. 1988, ApJ, 325, 128

Kormendy, J., & Bender, R. 1999, ApJ, 522, 772

Lauer, T. R. 1986, ApJ, 311, 34

Lauer, T. R., Bender, R., Kormendy, J., Rosenfield, P., & Green, R. F. 2012, ApJ, 745, 121

Li, Z., Wang, Q. D., & Wakker, B. P. 2009, MNRAS, 397, 148

Li, Z., Garcia, M. R., Forman, W. R., et al. 2011, ApJ, 728, L10

Li, Z., et al., 2014, in preparation

Mathis, J. S., & Cardelli, J. A. 1992, ApJ, 398, 610

Markwardt, C. B., 2009, ASPC, 411, 251M

McConnachie, A. W., Irwin, M. J., Ferguson, A. M. N., et al. 2005, MNRAS, 356, 979

Melchior, A.-L., Viallefond, F., Guélin, M., & Neininger, N. 2000, MNRAS, 312, L29

Melchior, A.-L., & Combes, F. 2011, A&A, 536, A52

Melchior, A.-L., & Combes, F. 2013, A&A, 549, A27

Menten, K. M., Reid, M. J., Forbrich, J., & Brunthaler, A. 2007, A&A, 474, 515

Massa, D., Savage, B. D., & Fitzpatrick, E. L. 1983, ApJ, 266, 662

Misselt, K. A., Clayton, G. C., & Gordon, K. D. 1999, ApJ, 515, 128

Morrissey, P., Conrow, T., Barlow, T. A., et al. 2007, ApJS, 173, 682

Nataf, D. M., Gould, A., Fouqué, P., et al. 2013, ApJ, 769, 88

Olsen, K. A. G., Blum, R. D., Stephens, A. W., et al. 2006, AJ, 132, 271

Peng, C. Y. 2002, AJ, 124, 294

Phillips, M. M., Simon, J. D., Morrell, N., et al. 2013, ApJ, 779, 38

Revnivtsev, M., van den Berg, M., Burenin, R., et al. 2010, A&A, 515, A49

Roming, P. W. A., Kennedy, T. E., Mason, K. O., Nousek, J. A., Ahr, L., Bingham, R. E., Broos, P. S., Carter, M., M., et al. 2005, Space Sci. Rev., 120, 95

Rosenfield, P., Johnson, L. C., Girardi, L., et al. 2012, ApJ, 755, 131

Rosolowsky, E. 2007, ApJ, 654, 240

Rubin, V. C., & Ford, W. K., Jr. 1971, ApJ, 170, 25

Saglia, R. P., Fabricius, M., Bender, R., et al. 2010, A&A, 509, A61

Schlafly, E. F., & Finkbeiner, D. P. 2011, ApJ, 737, 103

Sumi, T. 2004, MNRAS, 349, 193

Stark, A. A. 1977, ApJ, 213, 368

Udalski, A. 2003, ApJ, 590, 284

Valencic, L. A., Clayton, G. C., & Gordon, K. D. 2004, ApJ, 616, 912

Vázquez, G. A., & Leitherer, C. 2005, ApJ, 621, 695

Walterbos, R. A. M., & Kennicutt, R. C., Jr. 1988, A&A, 198, 61

This preprint was prepared with the AAS LaTeX macros v5.2.

A. Dependance of A_n/A_{F547M} on Background Spectrum

Compared with spectroscopic observations, broad-band photometric studies of the extinction curve do have certain drawbacks. For a dusty clump with certain extinction curve, the effective wavelength and hence the relative extinction, A_n/A_{F547M}, of a filter could depends on the shape of the background spectrum. If there is more emission in the shorter wavelength (for example, due to the presence of a young stellar population), the effective wavelength of the filter could then shift to the shorter wavelength and the A_n becames larger, and vice versa.

We use the stellar synthesis model, Starburst99 (Vázquez & Leitherer 2005), to examine the variation of the relative extinction (A_n/A_{F547M}) for various incoming spectra. Considering the high metallicity and no evidence for any recent star formation in the M31 bulge, we assume a background stellar population with solar or super-solar metallicity ($2.5Z_\odot$) and age from 100 Myr to 10 Gyr. First, we redden the spectra of instantaneous starbursts of different ages and/or metallicities by using the extinction curves of the MW, LMC or SMC and various absolute extinction E(B-V) ($=A_B - A_V$, hereafter EBV for short). Second, we convolve this reddened spectra with the transmission curves of the thirteen filters to derive the observed magnitude (m_n(EBV)) by using 'SYNPHOT' in 'IRAF'. Third, we fit the A_n(EBV) ($=m_n$(EBV)-m_n(0)) as a linear function of EBV to derive A_n/EBV, as well as $\frac{A_n}{A_{F547M}}=\frac{A_n}{EBV}\ /\ \frac{A_{F547M}}{EBV}$.

The ranges of A_n/A_{F547M} of the MW and the MCs for the instantaneous starbursts with solar metallicity are listed in Table. 6. For the *HST* filters, this ratio changes less than 6%. On the other hand, for the three UV filters of *Swift/UVOT*, this ratio is sensitive to the background stellar population and decreases by ∼45%, ∼17%, ∼25% for UVW2, UVM2 and UVW1 from 100 Myr to 10 Gyr. The 'Red Leak' problem of UVW2 and UVW1 (see §2.2) is the main reason to explain the large variation of A_n/A_{F547M} at these two bands. We also compare A_n/A_{F547M} between the $Z_\odot$ and $2.5Z_\odot$. Since the metallicity can significantly change the UV colors of the underlying stellar population, the systematic shift of A_n/A_{F547M} between the $Z_\odot$ and $2.5Z_\odot$ could reach ∼13% (UVW2 and UVM2) or 5.5% (UVW1) for the old stellar population, assuming the SMC extinction curve, which rises quickly in the UV bands. Instead, the change of A_n/A_{F547M} for the nine *HST* filters is less than 1% .

Considering the dependence of A_n/A_{F547M} on the background spectrum, in §5, we adopt the underlying stellar populations characterized by Dong et al. (2014). With the same *HST* dataset, Dong et al. (2014) divide the extinction-free region in the southeast of the M31 (see also Fig. 2) into concentric annuli of 5″ wide and fit the SED in each annulus individually with two metal rich instantaneous starbursts (intermediate-age: ∼700 Myr, $\sim 2Z_\odot$ and old: ∼12 Gry, $\sim 1.3Z_\odot$). They provide the radial profiles of ages and metallicities of these two

stellar populations along the minor axis of the M31 bulge, which we use to construct the intrinsic spectra of the background stellar population for our five dusty clumps. Then, we use the same method above to derive the model A_n/A_{F547M}, used to compared with the observed relative extinction in §5. For R_V=2.5, we calculate the standard deviation of A_n/A_{F547M} among the annuli between 10″ to 60″, which are 4.5%, 1.2%, 0.9% in the UVW2, UVM2 and UVW1 band, smaller than the observed uncertainties of these filters in §4.4.

B. Flattening Bias

We employ the method of Fritz et al. (2011) to remove the 'flattening bias'. The method is based on the following assumption: the intrinsic starlight and extinction distribution in the three UV filters could be mimicked from the other observations, such as the *HST* F336W image. Although the F275W band is closer to the three UV bands, it has larger photometric uncertainty, compared to the F336W band (see Table. 1).

We use the following steps to constrain the relative extinction of the *Swift/UVOT* filters in the CNR of M31. We assume that S_{F336W} derived in §4.1 is similar to the intrinsic light distribution of the three UV filters, the extinction distribution of which is also proportional to that of the F336W band, i.e. $A_n = \Gamma(n, F336W) \times A_{F336W}$. For the observed and intrinsic F336W images, we first set the 'source' pixels to 0 and then convolve the images with the *Swift/UVOT* PSF (§2.2). The new observed and intrinsic F336W images are used to derive $A(F336W)$ through the Eqn 1 (f from §4.3). Second, for a certain $\Gamma(n, F336W)$, we obtain a extinction map, A_n, which is used to redden the intrinsic F336W images. Third, for each *Swift/UVOT* pixels, we calculate the ratio of the sum of the reddened and intrinsic intensities of the corresponding *HST* pixels above. Fourth, we use 'MPFIT' to search for $\Gamma(n, F336)$ that best matches the above model ratio with the one between observed and intrinsic intensities of dusty pixels in *Swift/UVOT* images. The median and standard deviation of Γ(n,F336W) for each dusty clump are listed in Table 4.

C. Effect of the Scattered Light

We estimate the effect of the scattered light on our derived extinction curve. A derpojected Sérsic model, assumed to be sphereically symmetric, is adopted to approximate the radiation field in the M31 bulge. For a dusty clump inside the bulge, we derived I_s (the scattered intensity), I_{ua} (the total starlight intensity from the front side) and I_a (from the back side). The ratio, $\frac{I_s}{I_{ua}+I_a}$, represents the importance of the scattered intensity in

Eqn. 1. Groves et al. (2012) suggested that the dust is probably optical thin even in the near-UV wavelength. This is supported by our data: N_H never significantly exceeds 10^{21} H cm^{-2} (Li et al. 2014) and the optical depth should be smaller than 0.6 even in the UVM2 band. Therefore, for simplicity, we neglect multiple-scattering events.

We constructed the deprojected Sérsic model for the stellar light emissivity, $\nu(r)$ (in units of ergs s^{-1} cm^{-3}, where r is the physical radius, in units of pc) by using Eqn. 20a in Baes & Gentile (2011). According to Li et al. (2014), the average Sérsic index of the M31 bulge for the ten *HST* filters is ∼2.2, which is consistent with that obtained by Kormendy & Bender (1999). The effective radius of the Sérsic model is 313 pc. We calculated $\nu(r)$ for the central 1 kpc×1 kpc (i.e. $\sim 250'' \times 250''$ in projection) with a spatial resolution of L=4 pc. This region contributes ∼98% of the total starlight in the M31 bulge.

Then, we put a dusty clump into the model with different sky coordinate (R, z) to derive I_s, I_{ua}, I_a, and then $\frac{I_s}{I_{ua}+I_a}$. 'R' is the projected distance and 'z' is the line of sight distance, in units of pc. Both the 'R' and 'z' are centered at the nucleus. 'z' is the monofonic function of f. Since we knew the $\nu(r)$, for each 'z', we could derive the relative f. We adopted the extinction cross section per hydrogen ($\sigma_{ext}(n)$, cm^2/H) and differential scattering cross section per hydrogen ($\frac{d\sigma_{sca}(n,\theta)}{d\Omega}$, cm^2 H^{-1} sr^{-1}) from Draine (2003). We wrote the following equations:

$$I_{ua} \propto \sum_{z'>z(f)} L^3 \nu(r') \tag{C1}$$

$$I_a \propto \sum_{z'<z(f)} L^3 \nu(r') \times 10^{-0.4 \times N_H \times \sigma_{ext}(n)} \tag{C2}$$

$$I_s \propto \sum_{r'} \frac{L^3 \nu(r') \times L^2}{4\pi \times |r'-r|^2} \times N_H \times \frac{d\sigma_{sca}(n,\theta)}{d\Omega} \tag{C3}$$

$L^3\nu(r')$ is the stellar emission for a block at r'. $\frac{L^2}{4\pi \times |r'-r|^2}$ is the solid angle of the dusty clump ('r') toward the stellar intensity of the block at 'r''.

Through the above model, we derive $\frac{I_s}{I_{ua}+I_a}$ for our thirteen filters with different projected distances ('R' from 0 to 250 pc, i.e. 1.1′), f (0.2 to 0.9, with a binsize of 0.1) and absolute extinction (A_V, 0.1 to 0.7, with a bin size of 0.2) for MW-type dust (Draine 2003). Since $\sigma_{ext}(n)$ and $\frac{d\sigma_{sca}(n,\theta)}{d\Omega}$ of the SMC-type dust is smaller than those of the MW-type dust by nearly an order of magnitude (see Fig. 3 and Fig. 4 of Draine 2003), the effect of scattering for a SMC-type dust is much smaller than that of MW-type dust. In Fig. 8, we present $\frac{I_s}{I_{ua}+I_a}$ as a function of wavelength for our thirteen filters at two projected distances (100 pc and 250 pc) with four different f value (0.3, 0.5, 0.7 and 0.9). The $\frac{I_s}{I_{ua}+I_a}$ is larger in the shorter wavelength, because of the large extinction and scattering cross section. Since the

photons prefer forward-scattering (Draine 2003), the more starlight behind the dusty clump (larger f value), the more starlight will be scattered into the line of sight. When the clumpy is far away from the M31* (larger projected distance, 'R'), the I_{ua}+I_a decreases and more starlight from $r < R$ could be reflected to the lines-of-sight of observers.

We then used the above information to estimate the contribution of the scattered light in our five clumps. The averaged projected distances and f of the five clumps, derived by assuming that the scattered emission is negilible, are listed in Table. 3. Since our dusty clumps have either small projected distances (Clump A, B and C), small f (Clump E) or low absolute extinction (A_{F547M}, Clump D), we expected that the $\frac{I_s}{I_{ua}+I_a}$ should be roughly less than 5% in all our thirteen filters. We further quantified the effect of the scattered light on our results. From the averaged projected distance, f and median A_{F547M}, we derived $\frac{I_s}{I_{ua}+I_a}$ of the thirteen filters for each clump. Then, we divided $\Re$(n,k) in Eqn. 1 by $(1+\frac{I_s}{I_{ua}+I_a})$ to exclude the scattered emission. After reprocessing the steps in §4.3 and §4.4, we found that the f for the five dusty clumps decreases by less than 5% and the $\Gamma(n)$ changes less than 3% in the UV bands. Therefore, we concluded that the ignorance of the scattered emission in Eqn. 1 has little effect on our result.

D. Effect of Unresolved Reddening Structure in One *HST* Resolution Element

We use the extinction map of Orion molecular clouds from Kainulainen et al. (2009) to measure the bias introduced by unresolved dust structure in one *HST* resolution element. We first interpolate the intrinsic light distribution (S_n) at the F547M band in §4.1 into a finer pixel size (0.048″, ∼0.18 pc in the M31 bulge). Then, by using the extinction map from Kainulainen et al. (2009) and the f values listed in Table 3, we simulate the observed light distribution (I_n) in the five dusty clumps in Fig. 2 with Eqn. 1, which is then downgraded into the original pixel size of our *HST* images (0.13″). A_V in the Orion molecular cloud reaches 25 mag, much larger than those of our five dusty clumps. Thus we first scale the absolute extinction of the Orion molecular cloud to match the minimum $\Re_{F547M} = \frac{I_{F547M}}{S_{F547M}}$ of the simulated and real (§2.1) observed light distributions for each clump. We then estimate the uncertainty of the simulated observed light in individual pixels, from dispersion σ_n (see §2.1). We finally use the average relative extinction, $\Gamma(n)$, listed in Table 3, or the MW/SMC/LMC-type extinction curves, to get the A_n distribution at the other nine bands for each dusty clump and produce the simulated observed light distribution at these bands, with the same method above. Then, the similar steps used in §4.2 and §4.3 are used to calculate the f and $\Gamma(n)$ for these five dusty clumps. We find that the differences between the input and output values of f and $\Gamma(n)$ are less than 3% and 2%, respectively. This

means that thanks to the high resolution of our *HST* observations, we may resolve enough detail structures of the dusty clumps in M31 bulge. Therefore, we can neglect this effect due to the subpixel dust structure.

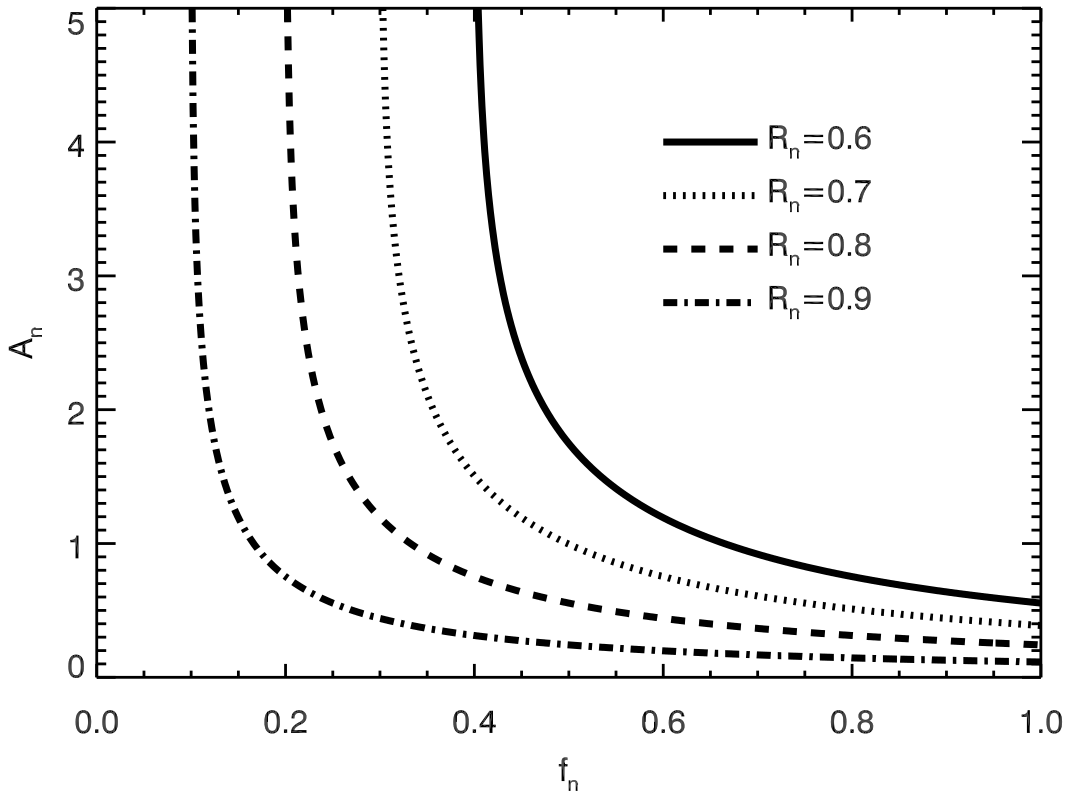

Fig. 1.— The relationship between the fraction of obscured starlight (f_n) and the absolute extinction A_n for different $\Re_n$=I_n/S_n derived from Eqn. 1 (I_n and S_n are the *observed* and *intrinsic* intensities). f is anti-correlated with A_n. When f_n decreases, (i.e., more stars in front of a dusty clump), A_n increases for the same $\Re_n$.

Table 1. Multi-Wavelength Filters

Filter	Detector	Central Wavelength (Å)	Width (Å)	Exposure	$< \sigma_n/I_n >^a$
UVW2	*Swift/UVOT*	1928	657	106 ks	
UVM2	*Swift/UVOT*	2246	498	46 ks	
UVW1	*Swift/UVOT*	2600	693	153 ks	
F275W	*WFC3* /UVIS	2704	398	925 s	8.6%
F336W	*WFC3* /UVIS	3355	511	1250 s	2.7%
F390M	*WFC3* /UVIS	3897	204	2700 s	2.8%
F435W	*ACS*/WFC	4319	1038	2200-4600 s	2.7%
F475W	*ACS*/WFC	4747	1458	1900 s	3.0%
F547M	*WFC3* /UVIS	5447	650	2700 s	3.6%
F665N	*WFC3* /UVIS	6656	131	2700 s	4.4%
F814W	*ACS*/WFC	8057	2511	1715 s	5.6%
F110W	*WFC3* /IR	11534	4430	699 s	9.3%
F160W	*WFC3* /IR	15369	2683	1600 s	11.1%

Note. — a) The median ratio of the empirical noise to observed intensity of the ten *HST* filters in the central $2' \times 2'$ ($\sim$450pc$\times$450pc) of M31 (see § 2.1).

Table 2. Five Dusty Clumps

Name	R.A. (degree)	Dec. (degree)	size
Clump A	10.683603	41.272742	$12.8'' \times 10.3''$
Clump B	10.695704	41.272921	$7.7'' \times 12.8''$
Clump C	10.677435	41.268105	$7.7'' \times 10.3''$
Clump D	10.681562	41.283549	$10.3'' \times 10.3''$
Clump E	10.700926	41.282015	$10.3'' \times 20.5''$

Table 3. Properties of the Five Dusty Clumps

	Clump A	Clump B	Clump C	Clump D	Clump E	Average
f	0.63±0.066	0.37±0.020	0.47±0.133	0.96±0.201	0.32±0.014	
$\Gamma(UVW2)^a$	2.54±0.387	2.57±0.913	3.62±0.627	3.22±0.340	2.43±0.419	2.87±0.380
$\Gamma(UVM2)$	2.99±0.360	3.93±0.554	4.94±0.736	4.68±0.462	3.45±0.952	3.92±0.502
$\Gamma(UVW1)$	2.41±0.211	2.88±0.512	2.88±0.414	2.65±0.429	2.50±0.344	2.61±0.091
$\Gamma(F275W)$	2.57±0.091	2.99±0.176	2.98±0.731	2.66±0.163	2.88±0.228	2.80±0.261
$\Gamma(F336W)$	1.91±0.038	1.90±0.053	2.00±0.180	1.96±0.058	1.91±0.049	1.92±0.029
$\Gamma(F390M)$	1.56±0.024	1.60±0.038	1.58±0.079	1.61±0.034	1.57±0.031	1.58±0.019
$\Gamma(F435W)$	1.38±0.018	1.40±0.028	1.34±0.042	1.35±0.023	1.36±0.023	1.37±0.018
$\Gamma(F475W)$	1.22±0.015	1.18±0.019	1.20±0.033	1.21±0.018	1.21±0.019	1.21±0.006
$\Gamma(F665N)$	0.71±0.016	0.74±0.025	0.75±0.031	0.74±0.017	0.71±0.016	0.73±0.013
$\Gamma(F814W)$	0.56±0.021	0.65±0.026	0.62±0.037	0.62±0.020	0.59±0.019	0.61±0.031
$\Gamma(F110W)$	0.30±0.027	0.58±0.041	0.49±0.075	0.50±0.025	0.48±0.027	0.46±0.094
$\Gamma(F160W)$	0.23±0.029	0.57±0.046	0.45±0.015	0.47±0.030	0.46±0.030	0.43±0.099
$\langle r \rangle^b$	65 pc	121 pc	80 pc	232 pc	235 pc	
$\langle A_{F547M} \rangle$	0.25±0.1	0.5±0.18	0.31±0.08	0.18±0.07	0.56±0.20	
$R^c_{V,Fit}$	2.4±0.06	2.4±0.08	2.5±0.13	2.4±0.07	2.5±0.07	2.4±0.05
$R^d_{V,Car}$	2.3±0.05	2.3±0.08	2.2±0.32	2.2±0.07	2.3±0.07	2.3±0.05
Number of *HST* pixels	837	499	202	555	863	
χ^2/d.o.f (d.o.f =9)	2.7	3.4	2.6	4.4	1.9	4.2

Note. — a) $\Gamma(n) = \frac{A_n}{A_{F547M}}$, the relative extinction. b) '$\langle r \rangle$' is the averaged projected distance of each clump to the M31*. c) The R_V values for the extinction curve model of Fitzpatrick (1999). d) The R_V values for the extinction curve model of Cardelli et al. (1989).

Table 4. The Extinction Relative to the F336W Band for the *Swift*/*UVOT* Filters

	Clump A	Clump B	Clump C	Clump D	Clump E
$\Gamma(UVW2, F336W)$	1.33±0.201	1.35±0.478	1.81±0.268	1.64±0.167	1.28±0.218
$\Gamma(UVM2, F336W)$	1.57±0.186	2.07±0.286	2.47±0.293	2.39±0.225	1.81±0.497
$\Gamma(UVW1, F336W)$	1.26±0.107	1.51±0.266	1.44±0.161	1.36±0.215	1.31±0.178

Table 5. Summary of Uncertainties in $\Gamma(n)$

Source	Type	Error
Foreground Galactic extinction	statistic	10%
Fraction of obscured star light	systematic	5%
Scattered light	systematic	5%
Unresolved Reddening Structure	systematic	2%

Table 6. The Range of A_n/A_{F547M} for Stellar Populations with Different Ages and Foreground Extinction Types

Filter	Milky Way	LMC	SMC
UVW2	1.60-2.65	1.56-2.56	1.68-3.29
UVM2	2.33-2.79	2.22-2.63	2.43-2.93
UVW1	1.67-2.20	1.63-2.12	1.78-2.38
F275W	1.92-2.03	1.87-1.96	2.09-2.21
F336W	1.62-1.62	1.61-1.61	1.73-1.74
F390M	1.47-1.48	1.42-1.42	1.54-1.55
F435W	1.30-1.33	1.26-1.29	1.34-1.37
F475W	1.17-1.20	1.15-1.18	1.19-1.23
F665N	0.79-0.80	0.86-0.86	0.76-0.76
F814W	0.58-0.59	0.71-0.71	0.56-0.57
F110W	0.33-0.33	0.37-0.38	0.24-0.25
F160W	0.20-0.20	0.20-0.20	0.15-0.16

Note. — The metallicity of the background instantaneous population is solar metallicity and the ages are from 100 Myr to 10 Gyr.

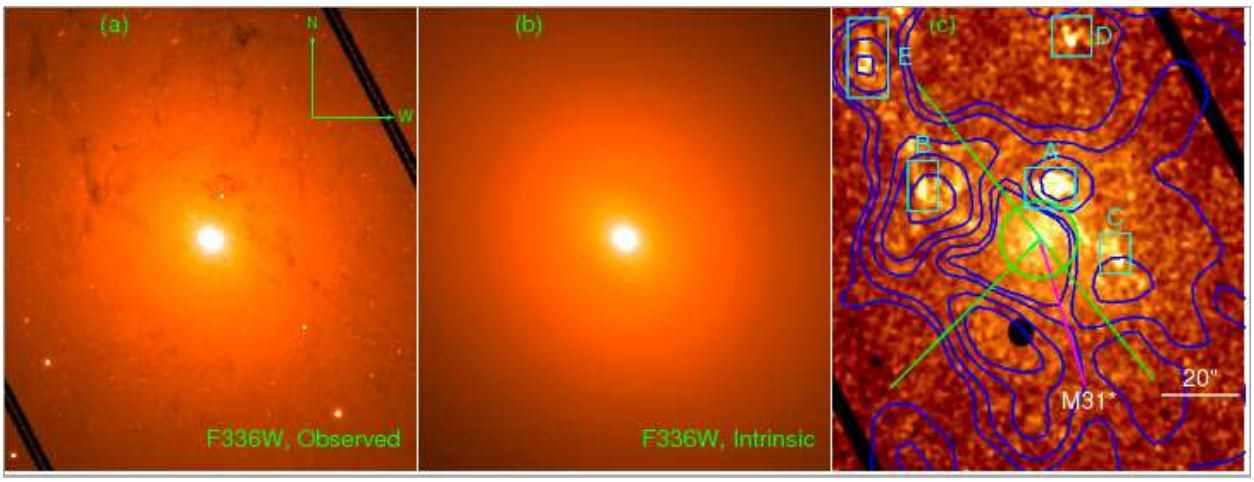

Fig. 2.— Left: *HST/WFC3* F336W intensity map of the central $2' \times 2'$ of the M31 bulge. Middle: The intrinsic light distribution of *HST/WFC3* F336W derived by the method in §4.1. Right: The intensity ratio map between the F160W and F336W bands, convolved with a Gaussian kernel of 9 pixels to reduce the noise. The five cyan boxes outline the dusty clumps used to constrain the extinction curves (see §4.3). The green circle shows the central $10''$ around the M31*. The black spot to the southeast is the 'death star' (very low sensitivity) feature in the *WFC3* /IR detector. The two black strips are excuded regions, which were covered by only one dithered exposure in the F275W or F336W bands and do not allow for cosmic-ray removal. The dashed and solid green lines represent the major and minor axes of the M31 bulge. The blue contours are from the Spitzer/IRAC 'dust-only' 8 μm intensity map of Li, Wang & Wakker (2009)

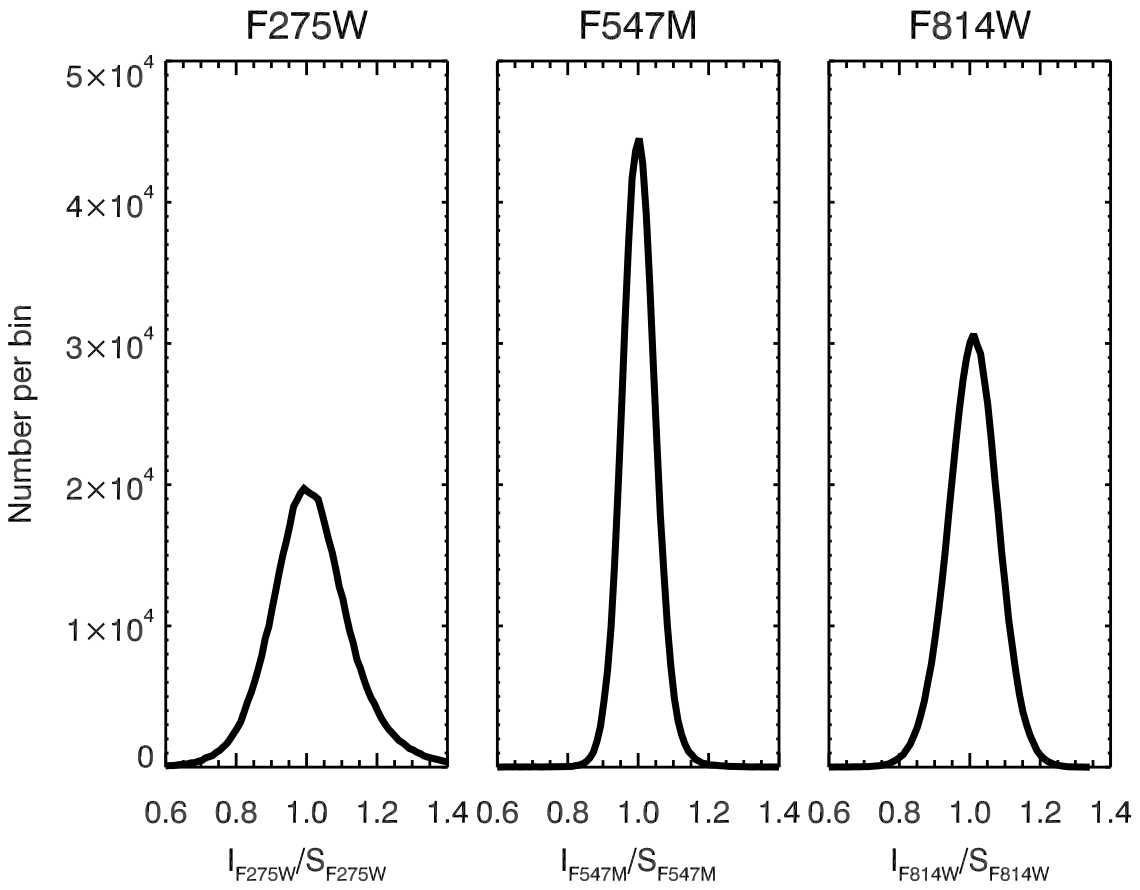

Fig. 3.— The distribution of I_n/S_n with a bin size of 0.01 for pixels in the central $2'\times2'$ of the M31 bulge at F275W, F547M and F814W. The curves can be fitted well by Gaussian functions, the centroid and standard deviation of which are ∼1 and 0.086/0.035/0.058 at F275W/F547M/F814W bands. The dispersions of the Gaussian functions can be explained by the photometric uncertainties at these three bands (σ_n, see Table. 1).

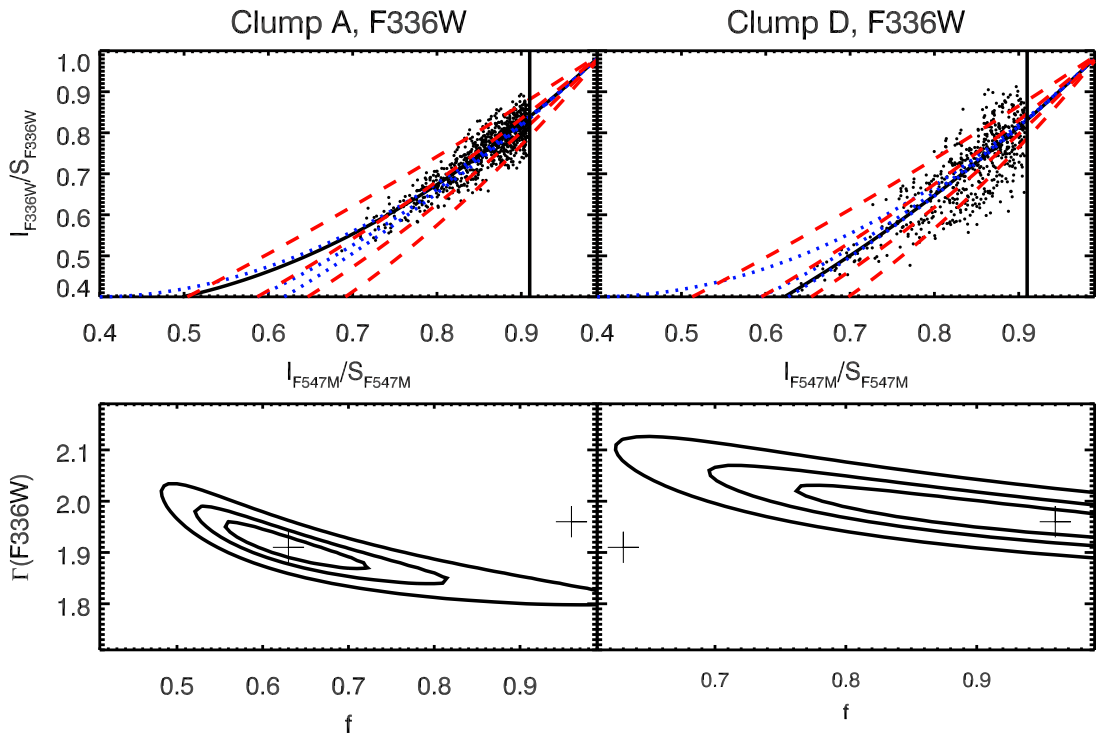

Fig. 4.— Top panels: I_{F336W}/S_{F336W} versus I_{F547M}/S_{F547M} for Clumps A (left) and D (right). The 'dots' represent the data points of individual 'dusty' pixels of the clumps. The cutoff for I_{F547M}/S_{F547M} around 0.9 is due to the criteria for selecting the 'dusty' pixels (vertical black lines). The solid lines represent the best-fit relationship (Eqn. 2, Clump A: f=0.63 and $\Gamma(F336W)$=1.91 and Clump D: f=0.96 and $\Gamma(F336W)$=1.96). The blue dotted lines represent the relationships with the best-fit $\Gamma(F336W)$ and f fixed at 0.6 (bottom),0.8 (middle) and 1.0 (top), whereas the red dashed lines represent the best-fit relationships with f and $\Gamma(F336W)$ fixed at [0.7 (top),0.9 (middle-up),1.1 (middle-low),1.3 (bottom)] $\times$ its best-fit value. For the 'dusty' pixels with $I_{F547M}/S_{F547M} > 0.85$, the I_{F336W}/S_{F336W} is not sensitive to f, but can constrain the $\Gamma(F336W)$. On the other hand, the observed data points with $I_{F547M}/S_{F547M} < 0.8$ can distinguish the different values of f. Bottom panels: f versus $\Gamma(F336W)$ for Clumps A (left) and D (right). The contours represent 60, 90 and 95% confidence levels. The 'plus' symbols mark the best-fit f and $\Gamma(F336W)$ for these two Clumps.

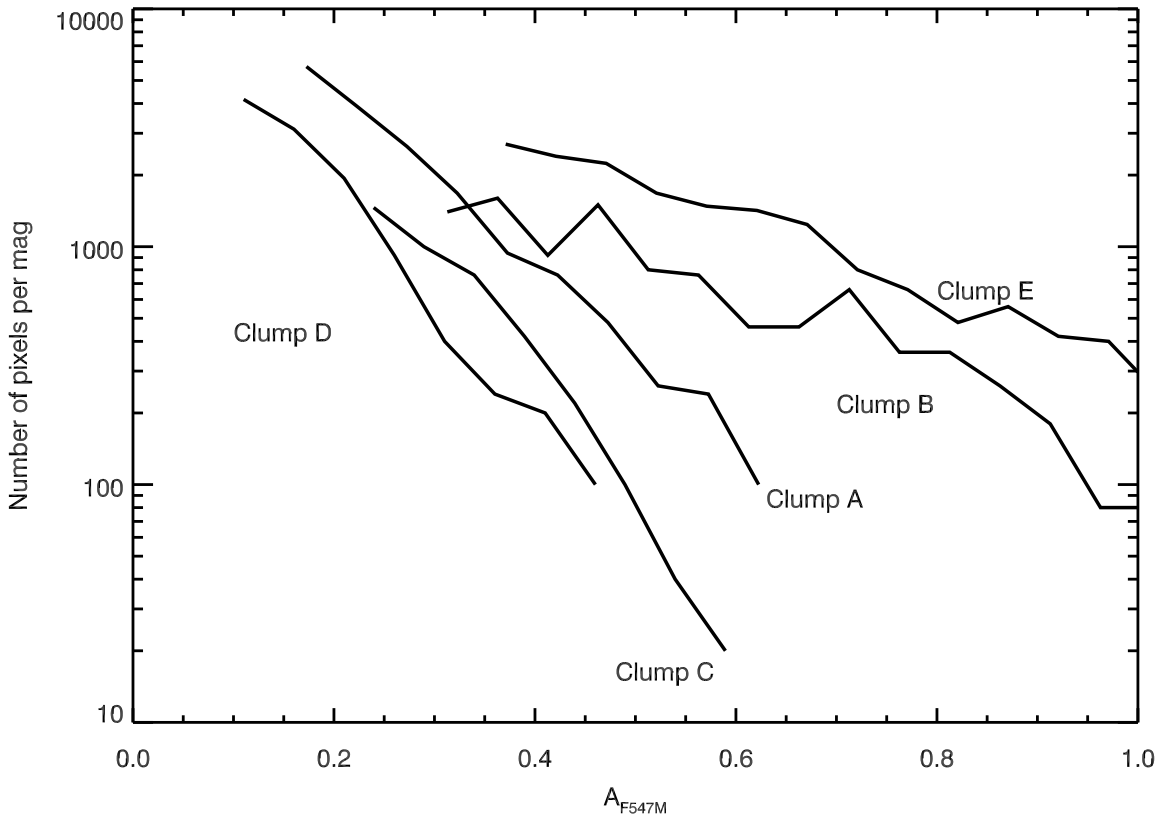

Fig. 5.— The A_{F547M} distribution of the 'dusty' pixels for the five clumps (see § 4.3). The bin size of the curves is 0.1 mag.

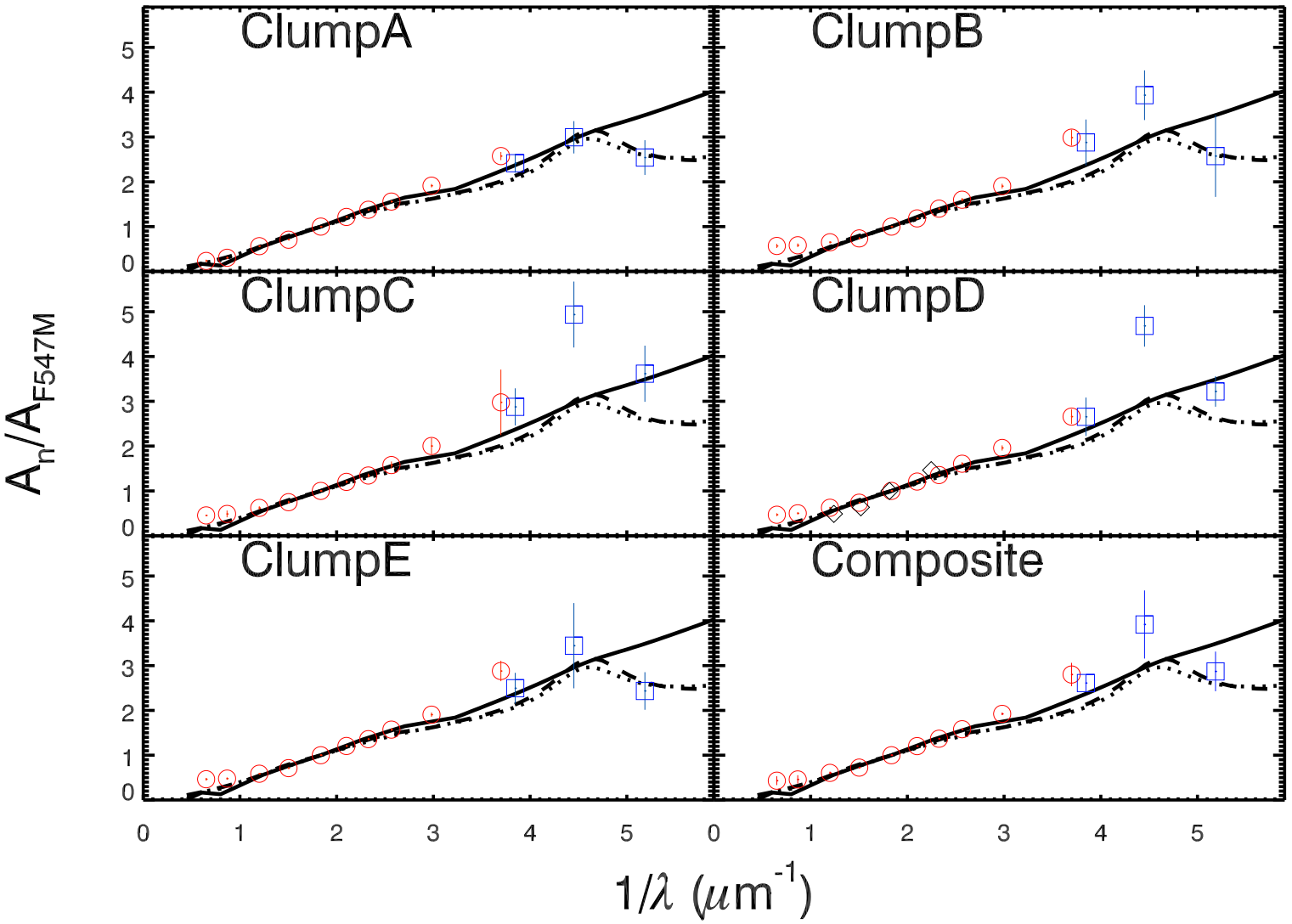

Fig. 6.— The relative extinction (A_n/A_{F547M}) of the five dusty clumps and the averaged one (the low-right panel). The red 'circle' and blue 'box' symbols represent *HST* and *Swift* filters, respectively. For comparison, the extinction curves of the SMC (solid), LMC (dotted) and MW (dashed) are also shown. The black 'diamonds' in the middle-right panel represent the A_n/A_V for the M31 bulge in Melchior et al. (2000). In the UV bands, $1/\lambda$ (μm^{-1}) $>$ 3.5, the extinction curves of our dusty clumps are steeper than that of the MW, even that of the SMC. Clumps C and D have large relatively extinction around 2175Å ($1/\lambda \sim 4.6$).

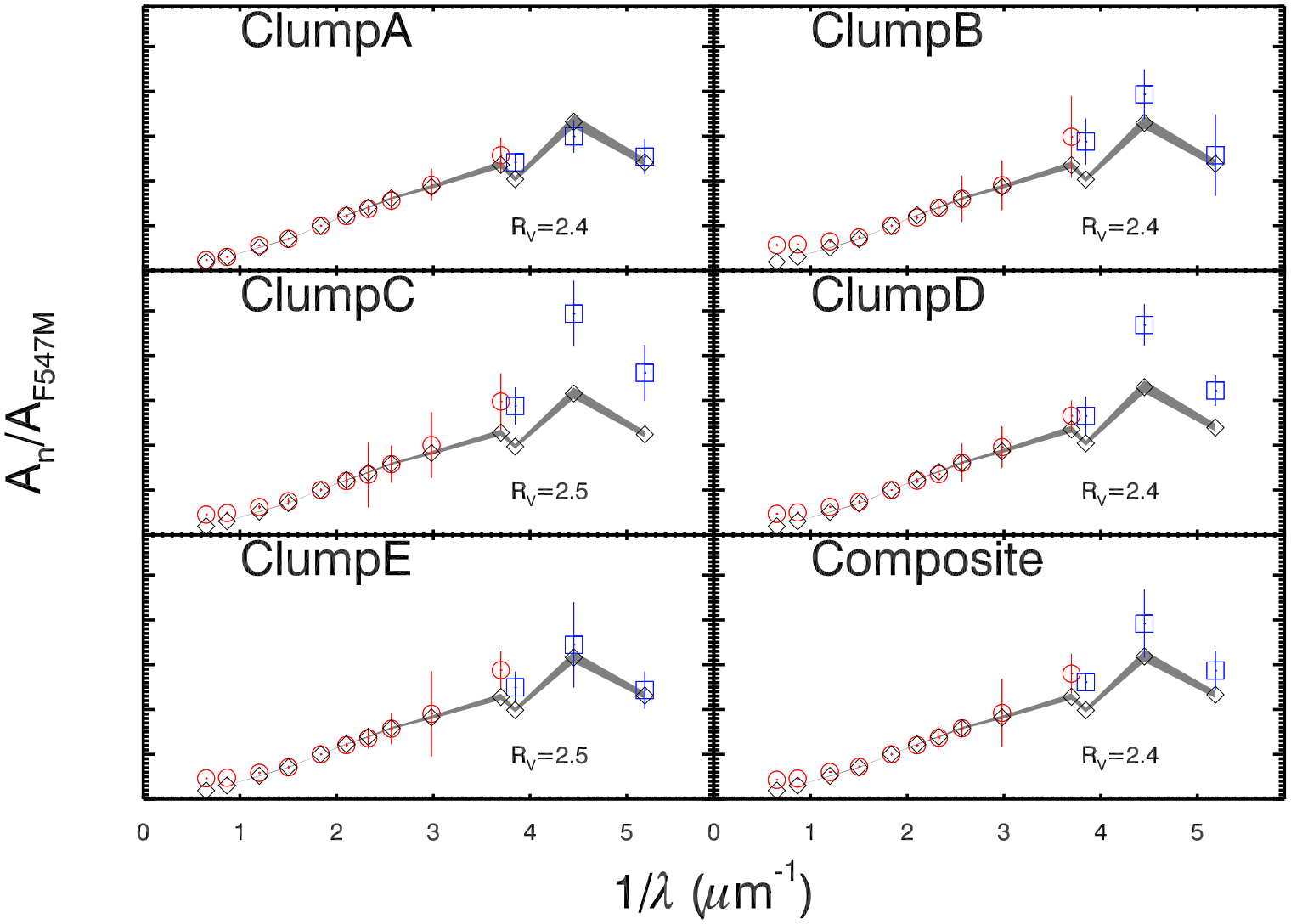

Fig. 7.— The same as Fig. 6, but compared with the A_n/A_{F547M} (diamonds) predicted by the Galactic extinction model of Fitzpatrick (1999) with the corresponding best-fit R_V obtained in §6. The shaded regions indicate the range of A_n/A_{F547M} with R_V equal to the best-fit $R_V \pm 0.1$. The R_V values are listed in the lower right corners of the panels. The extinction curves in the central 200 pc of the M31 bulge (R_V=2.4-2.5) are similar to the recent measurement toward the inner Galactic Bulge (R_V=2.5), which means that a steep extinction curve in the galactic bulge could be common.

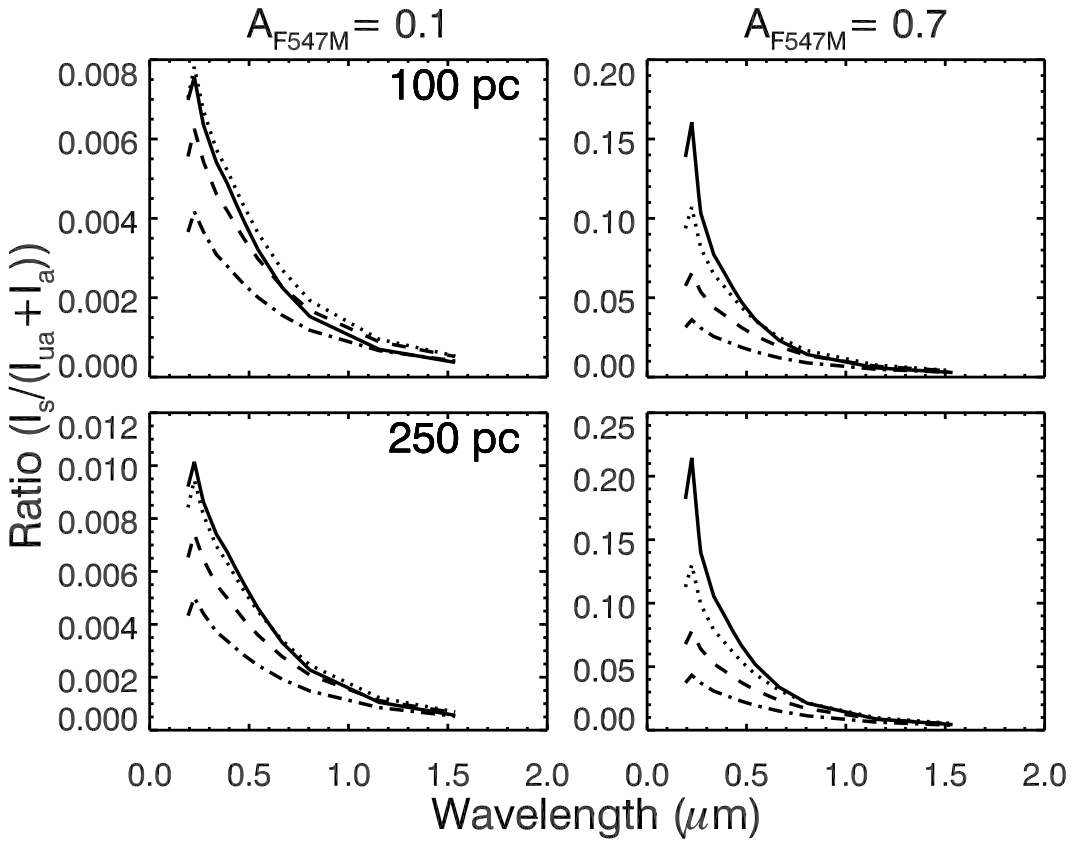

Fig. 8.— Illustration of the intensity ratio $\frac{I_s}{I_{ua}+I_a}$, as a function of the wavelength, the projected distance of a clump to the M31*, the fraction of obscured starlight (f) and absolute extinction (A_{F547M}). I_s, I_{ua} and I_a are the scattered light, the starlight in front of the dusty clumps and the obscured starlight. The top panels are for the projected distances 100 pc, while the bottom panel for 250 pc. The left column has A_{F547M}=0.1, while the right column has A_{F547M}=0.7. The lines in the plots from top to the bottom are for f = 0.9 (solid), 0.7 (dotted), 0.5 (dashed) and 0.3 (dash dot). The contribution of the scattered light, $\frac{I_s}{I_{ua}+I_a}$ decreases, following the increase of wavelength and the decrease of the projected distance/f/A_{F547M}. Considering the A_{F547M}, projected distances and f of our five dusty clumps, even at the three Swift/UVOT UV bands, the contribution of the scattered light is less than 5% .